

Rainfall Nowcasting From Multisatellite Passive-Sensor Images Using a Recurrent Neural Network

Frank Silvio Marzano, *Senior Member, IEEE*, Giancarlo Rivolta, Erika Coppola, Barbara Tomassetti, and Marco Verdecchia

Abstract—The term nowcast in hydrometeorology reflects the need for timely and accurate predictions of risky environmental situations, which are related to the development of severe meteorological events at short time scales. The objective of this paper is to apply a fully neural-network approach to the rainfall field nowcasting from infrared (IR) and microwave (MW) passive-sensor imagery aboard, respectively, geostationary Earth orbit (GEO) and low Earth orbit (LEO) satellites. The multisatellite space-time prediction procedure, which is named Neural Combined Algorithm for Storm Tracking (NeuCAST), consists of two consecutive steps. First, the IR radiance field measured from a geostationary satellite radiometer (e.g., Meteosat) is projected ahead in time (e.g., 30 min); second, the projected radiance field is used in estimating the rainfall field by means of an MW-IR combined rain retrieval algorithm exploiting GEO-LEO observations. The NeuCAST methodology is extensively illustrated and discussed in this paper. Its accuracy is quantified by means of quantitative error indexes, which are evaluated on selected case studies of rainfall events in Southern Europe in 2003 and 2005.

Index Terms—Neural network (NN), nowcasting methods, passive sensors, precipitation retrieval, satellite remote sensing.

I. INTRODUCTION

NOWCASTING of rainfall from remote sensing imagery is becoming an important issue for several applications, which are mainly related to civil protection alarming and also to hydrometeorological applications [1]–[4]. Multiple scales of space and time can be taken into account, as well as different data sources and objectives. The term nowcast should be intended, in this context, as the ability to predict, at very

short-term time scales, the evolution of the geophysical field of interest from remote sensing imagery. The satellite measurements used here implicitly define the time and space sampling imposed by the involved platform and sensor features [5]–[7]. For a rapidly varying field, such as rainfall, high temporal repetition of the observation, like that available from geostationary satellites, is essential [8]. On the other hand, the accuracy of the nowcasted fields is strictly related to the physical correlation of the measured remotely sensed data with the field of interest [9]–[11]. The rainfall nowcast problem from the satellite remote passive sensors can be conveniently split into two basic components as follows: 1) instantaneous retrieval; and 2) temporal prediction.

Several rain retrieval techniques have been proposed on the basis of multisatellite imagery, exploiting passive sensor measurements acquired by geostationary Earth orbit (GEO) and low Earth orbit (LEO) platforms [8]–[14]. These approaches tend to overcome some inherent limitations due to the use of satellite infrared (IR) radiances, which are poorly correlated with rainfall [6]. In this respect, microwave (MW) radiometric data available from LEO platforms can provide more accurate rain estimates [15]. From a microphysical point of view, visible (VIS) and IR radiometers can give information on cloud top layers since precipitating clouds are almost completely opaque in the IR. On the other hand, MW radiometers can detect cloud structure and, to some extent, near-surface rainfall. In fact, MW brightness temperatures are fairly sensitive to liquid and ice hydrometeors since rain clouds are not optically opaque at MW frequencies [16]. From a system point of view, GEO satellites can ensure an Earth coverage with a high temporal sampling, whereas LEO satellites have the advantage to enable the use of MW sensors but with the drawback of low temporal sampling. Therefore, LEO-MW and GEO-IR radiometries are clearly complementary in monitoring the Earth's atmosphere and a highly variable phenomenon such as precipitation. The IR radiances from geostationary images can be properly calibrated using the MW-based combined algorithms (e.g., [5] and [13]–[16]). Microwave data can be extracted from the MW imager sensors, but any rain estimation source may be used [9].

Rainfall nowcasting by active and passive remote sensing imagery has been attempted by numerous techniques in the last decade [3], [4], [17], [18]. Some of the proposed nowcast methods may be classified as standard, which are, hereafter,

Manuscript received August 14, 2006; revised March 19, 2007. This work was supported in part by the Interreg-III B RiskAWARE project, by the Civil Service Protection Directorate of Region Abruzzo, Italy, and by the Italian Department of Civil Protection, Rome, Italy.

F. S. Marzano and G. Rivolta are with the Department of Electronic Engineering, University of Rome "La Sapienza," 00184 Rome, Italy and also with the CETEMPS Center of Excellence, University of L'Aquila, 67010 L'Aquila, Italy (e-mail: marzano@die.uniroma1.it; giancarlo.rivolta@aquila.infn.it).

E. Coppola, B. Tomassetti, and M. Verdecchia are with the CETEMPS Center of Excellence, University of L'Aquila, 67041 L'Aquila, Italy (e-mail: marco.verdecchia@aquila.infn.it; barbara.tomassetti@aquila.infn.it; erika.coppola@aquila.infn.it).

Color versions of one or more of the figures in this paper are available online at <http://ieeexplore.ieee.org>.

Digital Object Identifier 10.1109/TGRS.2007.903685

also called “conventional,” such as the temporal image persistence (TIP), steady-state displacement (SSD), and linear temporal extrapolation (LTE) methods (e.g., [17]). Each of these conventional nowcasting methods shows a performance that depends on the weather conditions in the considered region. Neural networks (NNs) may present several advantages with respect to conventional techniques [19]. Their main feature is the ability to map input–output data to any degree of nonlinearity [20]. It is well known that the NNs exhibit the capability to learn and to represent highly nonlinear functional and to be quite robust to noise [21]. Moreover, if properly designed, an NN can be suitable to represent dynamical random processes such as the temporal evolution of a rain field [22].

The basic aim of this paper is to exploit the potential of an NN methodology to both predict and retrieve the rainfall pattern, having at disposal both GEO-IR and LEO-MW passive sensor data. Special attention has been placed to select the input space-time features and the network topology in order to optimize the rainfall nowcasting performance from the satellite imagery temporal sequences with respect to the conventional approaches. The focus of the proposed technique is on the design of an NN robust approach that is able to generalize the training data in an effective and efficient way. It is worth anticipating that a systematic validation of the Neural Combined Algorithm for Storm Tracking (NeuCAST) technique is beyond the scope of this paper.

This paper is organized as follows. In Section II, the overall rainfall nowcast procedure is introduced together with the main data sources. In Section III, a case study of an orographic rain event in Southern Europe is illustrated, and a temporal autocorrelation analysis of the IR radiance field is presented. Section IV is devoted to the design of the adopted NN topology, training algorithm, and input features. Sections V and VI show the results, in terms of error statistics, obtained for the nowcasting of the IR radiance field and for the rain retrieval, respectively, derived by applying a multisatellite radiometric NN-based algorithm to selected case studies. Conclusions are finally drawn in Section VII.

II. SATELLITE NOWCAST OF RAINFALL FIELDS

After describing the overall rainfall nowcast approach, three conventional forecast methods will be considered for comparison and will be briefly described.

A. Overview of the Rainfall Nowcasting Approach

Rainfall is a highly variable field with a fairly rapid and detailed space-time scale of evolution, mainly depending on its stratiform or convective features (e.g., [23] and [24]). These field characteristics raise a question about the approach to the nowcast problem; that is, whether to predict either the radiance or rain-rate field. After various attempts, we have finally decided to opt for the prediction of the IR brightness temperature (T_b) fields followed by the rainfall retrieval stage. This approach has several advantages with respect to the reverse

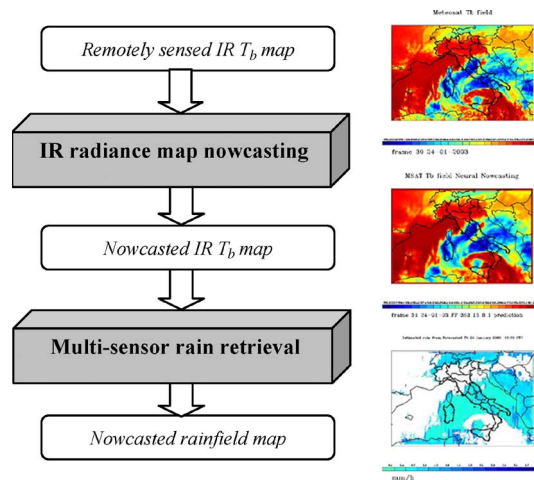


Fig. 1. Overall approach, which is named NeuCAST, to IR T_b nowcasting and rainfall retrieval from the multisatellite passive-sensor imagery.

approach (i.e., first, estimate the rain map and, then, predict it from the rain map itself).

- 1) It avoids the prediction errors connected to the delineation of the rainfall areas by a masking procedure.
- 2) It is not strictly connected to rain areas, thus smoothing the problem of predicting raincells from zero-rainfall pixels.
- 3) It allows the generation of other meteorological subproducts, starting from the predicted T_b field.

The proposed satellite-based nowcasting approach, which is named NeuCAST, can be schematically visualized in Fig. 1.

As a source of GEO satellite imagery, the Meteosat-7 VIS-IR Imager (VIRI) has been considered here, selecting areas of interest in Southern Europe (e.g., [9]). The selected IR Meteosat-7 image frames are composed of 547×298 pixels, corresponding roughly to east longitude ranging from 0° to 22° and north latitude ranging from 36° to 48° (see small panels in Fig. 1). Each VIRI pixel can be approximated by a square of 5×5 km² at midlatitudes. The Special Sensor Microwave/Imager (SSM/I), e.g., [25], [26], has been selected as the data source from the LEO satellites. The SSM/I MW radiometer operates on Defense Meteorological Special Program (DMSP) satellites and has four frequencies at 19.3, 22.2, 37.0, and 85.5 GHz. All channels are dual-polarized, except the 22.2-GHz feed that works at vertical polarization only. The SSM/I radiometer has a conical scan and a swath of 1400 km. For each scan, it takes 128 uniformly spaced samples at 85-GHz frequency with a spatial sampling of 12.5 km. At the other frequencies, data are sampled with a double spatial sampling, i.e., 25 km.

Other combinations of available sensors can be, of course, considered such as the Spinning-Enhanced VIRI Aboard Meteosat Second Generation (MSG), the Advanced Microwave Scanning Radiometer Extended (AMSR-E) aboard the Aqua satellite, and the SSM Imager Sounder (SSM/I/S) aboard the DMSP satellite. The generalization of the proposed approach to a larger combination of sensors and satellites is, however, not the aim of this paper, whose goal is to explore the feasibility of a

new neural nowcasting technique. Nevertheless, this extension is methodologically quite straightforward.

B. Conventional Nowcasting Methods

Three nowcasting techniques, which are called “conventional,” have been considered as benchmarks, following [17].

- 1) The first technique is the TIP method. This method assumes that the same value of the previous image can be associated to each pixel in the forecasted satellite image [17]. This means that, if the latest available (or current) image is the frame at the time step t_k , the forecasted satellite image, or frame, at the time step t_{k+1} is assumed to be equal to the frame at t_k .
- 2) The second technique is the SSD method. It assumes that the patterns in the satellite frame at t_k are transported (displaced) with unchanged size and intensity [17]. The frame at the time step t_{k+1} (or nowcasted image) is assumed to be equal to the last available satellite image, which is translated by a suitable motion vector. This displacement vector is found by calculating the temporal cross-correlational index between the frames at the time steps t_k and t_{k-1} for all the possible shifts between the two images within a range of $\pm N_s$ pixels (with N_s maximum here equal to eight and typically between zero and three).
- 3) The third technique is the LTE method. This method consists of linearly extrapolating in time the future pixel value [17]. The IR temperature associated with each pixel in the frame at the time step t_{k+1} is linearly derived from the values associated to the same pixel in the last two available images (i.e., frames at the time steps t_k and t_{k-1}).

III. CASE STUDIES OF RAINFALL EVENTS

In the following paragraphs, we will briefly describe the case studies used in testing our nowcasting technique and, then, briefly present a statistical analysis of the temporal autocorrelation of the measured IR radiance field.

A. Selected Precipitation Events Over Southern Europe

On January 23, 2003, in the Gulf of Genoa, a cyclogenesis was associated with a secondary minimum, which is located on the medium Adriatic Sea [18], [26]. At the upper levels, an intrusion of cold air from north to east, which is associated with a trough extending from Scandinavia to the southern Mediterranean region, was present. The low-level advection of warm and humid air from south to east into the Adriatic region caused the generation of diffuse convective precipitation. The following 24 h was characterized by the deepening of the surface pressure minimum, which is located in the south-central Tyrrhenian Sea. At the upper levels, a cutoff low was developing associated with a cold-air intrusion. Electrical activity was still detected during the night in the central and southern Adriatic Sea, suggesting that the convective activity was still underway over central Italy. An example of the Meteosat-7 IR radiance image

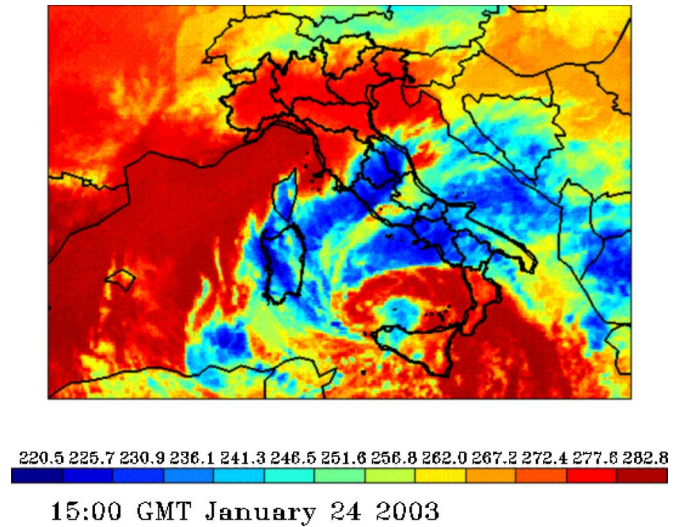


Fig. 2. Radiance field, which is represented in terms of the IR brightness temperature, measured from Meteosat on January 24, 2003, at 15:00 GMT (frame 30).

on January 24, 2003, at 15:00 Greenwich Mean Time (GMT) is shown in Fig. 2, where the high-cloud cyclonic structure in the Tyrrhenian Sea is clearly captured from the geostationary satellite.

On January 25, 2003, the upper level cutoff low was completely in phase with the surface low and located over Sicily. Low-level advection of warm and humid air over southern Italy produced convection with intense electrical activity. During the following 24 h, the cyclonic system moved toward the east. Data recorded by surface sensors clearly showed rainfall that persisted over central Italy during the whole period. The maximum rainfall rate, which is measured by most available rain-gauge stations (hourly sampling tipping buckets) in central Italy, did not exceed 20 mm/h, even though, over the Adriatic regions, rain-gauge values exceeding 45 mm/h were recorded both at the beginning and at the end of the event. The spatial and temporal distributions of rainfall during the event suggest the formation of so-called orographic precipitation with an embedded localized convective rainfall.

An additional comparison of the performances of the considered nowcasting techniques has also been performed on a sequence of satellite images from a case study on November 25–26, 2005. This event is a typical mid-Atlantic frontal system which caused several localized thunderstorms embedded in widespread rain along the Apennine range. This further example is considered in assessing the generalization capability of the considered prediction methods.

B. Statistical Analysis of Observed Radiance Field

A radiance field nowcast approach should try to exploit both the spatial texture and temporal memory of the observed events. It is worth investigating whether or not the knowledge of the dynamic structure of the radiance field can provide measurable added value to the nowcasting capability. Let us consider the IR brightness temperature field $T_b(x, y, t)$ in a given position

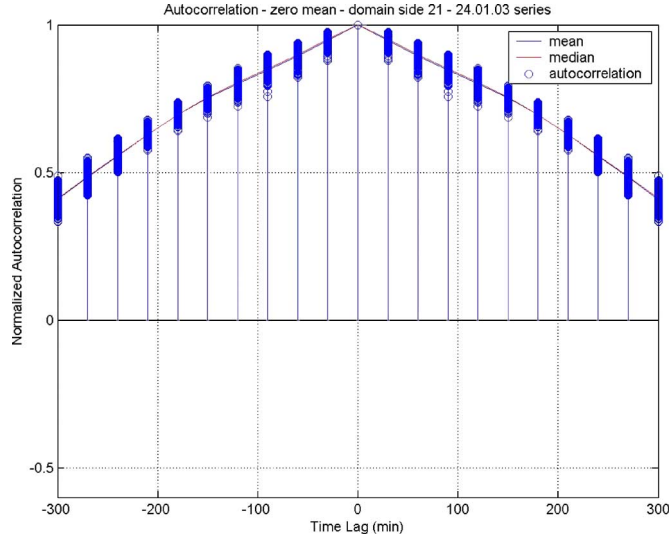


Fig. 3. Normalized autocorrelation of IR T_b related to fair weather condition pixels, extracted from the 48 Meteosat frames on January 23, 2003. Mean and median values of normalized autocorrelation are also plotted.

(x, y) of the satellite image as a function of time t . The temporal autocorrelation function C_T of such process is

$$C_T(x, y, \tau) = \int_{-\infty}^{+\infty} T_b(x, y, t)T_b(x, y, t + \tau)dt \quad (1)$$

where τ is the time delay. Let us consider a finite temporal series of N radiance field images, sampled every $\Delta\tau = 30$ min at a given discrete pixel (x_i, y_j) . Furthermore, let us take the function describing the discrete process as an anomaly around its mean

$$T'_b(x_i, y_j, t_k) = T_b(x_i, y_j, t_k) - \langle T_b(x_i, y_j) \rangle \quad (2)$$

where $\langle T_b(x_i, y_j) \rangle$ is the mean IR brightness temperature over the considered time interval. We can estimate the normalized temporal autocorrelation of this process at each time lag $\tau_l = l\Delta\tau$, with $l < N$, as

$$C_{nT}(x_i, y_j, \tau_l) = \frac{\sum_{k=1}^{N-l} T'_b(x_i, y_j, t_k)T'_b(x_i, y_j, t_k + \tau_l)}{\sum_{k=1}^N [T'_b(x_i, y_j, t_k)]^2} \quad (3)$$

for $\tau_l \geq 0$, and $C_{nT}(x_i, y_j, \tau_l) = C_{nT}(x_i, y_j, -\tau_l)$ for $\tau_l < 0$.

Considering a small area of 21×21 pixels (i.e., about 105×105 km²) within the available series of Meteosat images, the autocorrelation C_{nT} of the IR brightness temperature time series, which is associated to each pixel (x_i, y_j) belonging to a subdomain centered at (42° N, 14.5° E) within the central Adriatic region, has been estimated for two different meteorological conditions. In Fig. 3, C_{nT} for fair weather conditions is represented for each selected pixel. The mean and the median of these estimates are also shown for each time lag. This time series comprises the 48 satellite images series of January 23,

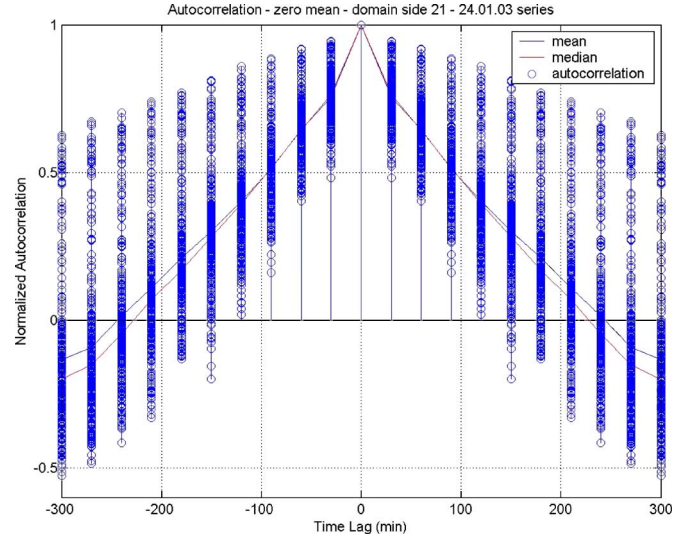


Fig. 4. Same as in Fig. 3 but for severe weather conditions, extracted from the 48 Meteosat frames on January 24, 2003.

2003. In the considered subdomain, there are no particularly rapid variations in the IR T_b field during this period. The result is a slowly decreasing autocorrelation sequence with a relatively small spread around the mean value. The mean of C_{nT} decreases to 0.5 after about 5 h.

Fig. 4, similarly to the previous figure, shows C_{nT} for the time series comprising the 48 satellite images series on January 24, 2003, on the same subdomain previously considered. This images series contains a severe convection, lasting several hours with an average precipitation in the range of 10 mm/h. The mean of the related autocorrelation sequence decreases more rapidly in this case, and the spread of C_{nT} values at each time lag appears to be noticeably higher. The mean of C_{nT} decreases to 0.5 after about 1.5 h.

In order to provide the nowcasting method with information related to the process space-time dynamics, it is also useful to introduce spatial texture information around the considered pixel. This means to assume that IR T_b , at a given target pixel and time, may depend on the IR T_b within an area comprising the same target pixel and its surroundings for some tens of kilometers (i.e., 10 to 50 km of “influence” radius) in the previous time steps. An effective way to deal with the space-time image information for estimation purposes in a strongly nonlinear and hybrid context is to resort to an NN approach, as described in the next section.

IV. RECURRENT (RC)-NN METHODOLOGY

It is well known that artificial NNs exhibit the capability to learn and to represent highly nonlinear relationships [20]. An NN, which is properly configured, can be regarded to as a universal function approximator [21]. In general, NNs provide a powerful methodology to predict temporal series associated with random processes. The proposed field nowcasting techniques are based on NN architectures, which are trained on a proper batch of GEO satellite images. We have considered here two major classes of NN topologies: the feedforward (FF) and the RC-NN [20].

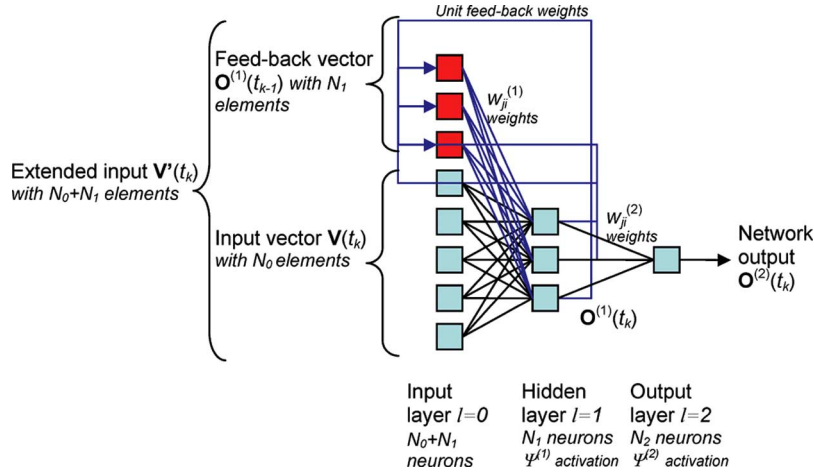


Fig. 5. Example of an Elman RC-NN topology with three layers and one output neuron. $\mathbf{V}(t_k)$ is the N_0 -size input vector at time t_k , while $\mathbf{V}'(t_k)$ is the $N_0 + N_1$ -size extended input vector comprising the delayed fed-back vector from the layer 1 output at time t_{k-1} and the synchronous input vector $\mathbf{V}(t_k)$.

An FF-NN computes an output pattern in response to an input pattern (IP) [20]. Once trained and set with proper connection weights, the output response to a given IP will be the same regardless of any previous network activity. The FF-NN response can be thought as a single instantaneous nonlinear mapping. On the other hand, the RC-NN response to a given IP will depend on the previous network activity, since such networks consist of processing units with dynamic elements and operate in time-lagged feedback mode [22].

A. RC-NN Architecture

A multilayer RC-NN is basically an extension of an FF-NN topology, which is widely described in the literature (e.g., [20] and [21]). A well-known topology of an RC multilayer NN is the Elman network [22]. It is commonly a multiple-layer network with a feedback from the last hidden layer output to the first hidden layer input (the layers between the input and the output layers are called hidden). The RC connections allow the Elman network to both detect and track the time-varying patterns. In addition to the RC connections, this type of NN is characterized, as is the FF-NN, by the forward propagation of the input information through the various layers. All neurons in a layer are connected to all neurons in the adjacent layers through synaptic weights which act as signal multipliers on the corresponding interconnections.

A three-layer Elman network is shown in Fig. 5. The neurons are grouped in sequentially connected layers with the layers numbered as $l = 0$, $l = 1$, and $l = 2$. In addition, the output of each neuron in the hidden layer ($l = 1$) is fed back, as an additional neuron in the input layer, to the input of each neuron of the hidden layer. The last layer ($l = 2$) is the output layer. The latter has only one neuron since the objective of this paper is to forecast the IR temperature associated to a given pixel x_i, y_j .

In case of a multilayer topology, let us first consider an FF network with $n + 1$ layers (with the layer index l ranging from 0 to n), each layer having N_l neurons (with the neuron index i_l in the layer l ranging from 1 to N_l). Provided an input vector

$\mathbf{V}(t_k)$ with N_0 elements $V_{i_0}(t_k)$, the output of the i_n th neuron of the output layer $l = n$ in an FF-NN is

$$\begin{aligned}
 O_{i_n}^{(n)}(t_k) = & \psi^{(n)} \left(\sum_{i_{n-1}=1}^{N_{n-1}} w_{i_n i_{n-1}}^{(n)} \psi^{(n-1)} \right. \\
 & \times \left(\sum_{i_{n-2}=1}^{N_{n-2}} w_{i_{n-1} i_{n-2}}^{(n-1)} \psi^{(n-2)} \dots \right. \\
 & \left. \left. \left(\sum_{i_1=1}^{N_1} w_{i_2 i_1}^{(2)} \psi^{(1)} \left(\sum_{i_0=1}^{N_0} w_{i_1 i_0}^{(1)} V_{i_0}(t_k) \right) \dots \right) \right) \right)
 \end{aligned} \quad (4)$$

where $\Psi^{(l)}$ is the activation function, which is assumed to be a sigmoid function, of the l th layer.

When the previous FF architecture is modified to represent the corresponding RC-NN (see Fig. 5), (4) needs to be changed accordingly. The number of elements in the input layer is increased due to the presence of a feedback connection from each output of the last hidden layer. The output of the i_n th neuron of the output layer $l = n$ can be expressed as follows for the RC-NN:

$$\begin{aligned}
 O_{i_n}^{(n)}(t_k) = & \psi^{(n)} \left(\sum_{i_{n-1}=1}^{N_{n-1}} w_{i_n i_{n-1}}^{(n)} \psi^{(n-1)} \right. \\
 & \times \left(\sum_{i_{n-2}=1}^{N_{n-2}} w_{i_{n-1} i_{n-2}}^{(n-1)} \psi^{(n-2)} \dots \right. \\
 & \left. \left. \left(\sum_{i_1=1}^{N_1} w_{i_2 i_1}^{(2)} \psi^{(1)} \left(\sum_{i_r=1}^{N_0+N_{n-1}} w_{i_1 i_r}^{(1)} V'_{i_r}(t_k) \right) \dots \right) \right) \right)
 \end{aligned} \quad (5)$$

where $V'_{i_r}(t_k)$ is an element of the extended input vector $\mathbf{V}'(t_k)$, as in Fig. 5. The previous expression has the same

structure as (4) but with a different argument of the activation function $\Psi^{(1)}$ for each neuron in the first hidden layer $n = 1$ in order to take into account the increased number of elements in the input layer. As a matter of fact, $V'_{i_r}(t_k)$ is the i_r -th element of the extended input vector with $N_0 + N_{n-1}$ elements, composed by the synchronous vector $\mathbf{V}(t_k)$ of N_0 elements and the delayed output vector $\mathbf{O}^{(n-1)}(t_{k-1})$ of N_{n-1} elements, which are the outputs of the neurons in the last hidden layer $l = n - 1$. Thus, in (5), the argument of the activation function $\Psi^{(1)}$ of the i_1 -th neuron in the first hidden layer can be explicitly written as

$$\sum_{i_r=1}^{N_0+N_{n-1}} w_{i_1 i_r}^{(1)} V'_{i_r}(t_k) = \sum_{i_r=1}^{N_0} w_{i_1 i_r}^{(1)} V_{i_0}(t_k) + \sum_{i_r=N_0+1}^{N_0+N_{n-1}} w_{i_1 i_r}^{(1)} O_{i_{n-1}}^{(n-1)}(t_{k-1}). \quad (6)$$

It is worth noting that $O_{i_{n-1}}^{(n-1)}(t_{k-1})$ does not uniquely depend on its synchronous vector $\mathbf{V}(t_{k-1})$ but also on its delayed vectors $\mathbf{O}^{(n-1)}(t_{k-l})$ with $1 < l \leq k - 1$ or, in other words, on the ordered input sequence $\mathbf{V}(t_1), \dots, \mathbf{V}(t_{k-1})$. This means that, for the first time step t_1 , the delayed feedback vector is not defined, so that the training of an RC-NN is forced to partially lose the initial pattern with respect to an FF-NN. However, the NN architectures are known to be quite robust to incomplete or erroneous IPs [27].

As an example, the output of the neuron in the last layer of the RC-NN in Fig. 5 can be calculated at the sequence step t_k using (5) with $n = 2$ and $N_0 = 5$, $N_1 = 3$ and $N_2 = 1$. The neuron index i_1 ranges from 1 to 3, whereas the neuron index i_0 ranges from 1 to 5 and the neuron index i_r ranges from 1 to 8. The neuron index i_2 for the layer $n = 2$ can be omitted since there is just one neuron in this layer.

B. NN Training Strategy

In order to determine the optimal weight vectors \mathbf{w} in (4) and (5), an NN is usually trained by minimizing the error function E using the steepest descent gradient backpropagation algorithm [20]. The weight increments Δw_{ij} are updated during the training in accordance with

$$\Delta w_{ij}(t_s) = -\alpha \frac{\partial E}{\partial w_{ij}} + \beta \Delta w_{ij}(t_s - 1) \quad (7)$$

where α and β are the learning rate and the momentum parameter, respectively, E is the error function, and t_s is the training step. The second term in (7) is a regularization term which helps in improving the NN convergence rate and the stability by damping oscillations [20].

An appropriate training strategy is needed to modify α and β during the learning process [28]. The optimal means of modifying these training parameters has not been determined, and therefore, a sensible but *ad hoc* approach is taken, in line with the approaches used by other authors [28], [29]. Specifically, the assumption is that the minimum of the error function in the

multidimensional parameter space is at the bottom of a wide and deep “valley,” and therefore, the learning phase is started with a large value of α . The learning strategy consists of two steps. In the first step, a large starting value of the learning rate (e.g., $\alpha = 0.2$) allows the exploration of a wide domain of the error-function space. The value of β is usually fixed at 0.8 and is not varied during the training process. The learning rate α does not decrease significantly until a wide and (supposedly) deep valley in the parameter space is detected. Then, the learning rate is gradually decreased until the incremental variation in (7) is negligible. In this way, the search of the global minimum is speeded up, and the probability of being trapped in a local minimum is minimized. In other words, the hypothesis is that the most probable absolute minimum of the error function E in the phase space is located at the bottom of the widest hole, since such a hole is usually the deepest one. Several trial and error tests have shown that this adaptive approach provides a faster training process and a better network final performance.

C. NN Training and Test Datasets

Both FF- and RC-NNs were trained to forecast the IR brightness temperature value $T_b(x_i, y_j, t_{k+1})$ associated with a given pixel (x_i, y_j) of the satellite image, starting from the measured values in a region around that pixel in the previous satellite images at time t_k and before.

Separate sequences of images for training and cross-validation were selected from the available set of Meteosat imagery; the remaining data were set aside for testing. A typical strategy in optimizing the NN, known as “early stopping” technique, has been used [21]. The reason for such a label is the following: when training an NN, the error reaches a minimum value on independent (cross-validation) data before it reaches a minimum value on the (dependent) training data; hence, training is stopped “early” relative to where would have been stopped, if only the error on training data had been monitored.

A time series of 15 satellite images (frames 4–18) on January 24, 2003, was used to extract $N_e = 2\,118\,540$ (from 2445090 available pixels) input and output T_b examples, utilized for the training (choosing 90% of pixels) and cross-validation (choosing the remaining 10% of pixels) stages.

In order to retain the IR image texture, the input vector $\mathbf{V}(t_k)$ of N_0 elements of IR T_b 's (see Fig. 5) was chosen with a variable number of elements. A square area around the given pixel (x_i, y_j) of 3×3 pixels was first selected. This means that N_0 ranged from $N_p = 9$ pixels, corresponding to a neighbor contour n_c of order 1 (i.e., $n_c = (\sqrt{N_p} - 1)/2 = 1$), to $N_p = 441$ elements, corresponding to $n_c = 10$ or a square area of 21×21 pixels. The optimal match of the NN topology and the input vector $\mathbf{V}(t_k)$, or rather the numbers N_e , N_0 , N_l , and n_c , were based on the results of a sensitivity test discussed in the next section.

The goal of the independent test stage was to predict the entire IR image (i.e., T_b values for all pixels) at time step t_{k+1} . The test stage was performed on the following: 1) a sequence of eight images (frames 3–10) available on January 24, 2003; 2) a sequence of eight images (frames 3–10) available on January 25, 2003; and 3) a sequence of eight images

(frames 26–33) available for a completely different case study on November 25, 2005.

V. IR RADIANCE FIELD NOWCASTING

The performances of different NN architectures were evaluated by means of statistical indexes and compared to the performances of conventional methods. The error bias m_ε (in kelvin), root-mean-square error (rmse) s_ε (in kelvin), and correlation index r_ε are defined in (8)–(10), shown at the bottom of the page, where $\hat{T}_b(x_i, y_j, t_k)$ and $T_b(x_i, y_j, t_k)$ are the nowcasted and measured T_b 's in a given pixel x_i, y_j at a given time t_k , respectively, N_{lon} and N_{lat} are the number of pixels along the directions x and y , and $\langle \hat{T}_b(t_k) \rangle$ and $\langle T_b(t_k) \rangle$ are the mean values of the nowcasted and measured T_b 's in the satellite image at a given time t_k .

The RC-NN requires a proper training batch, structuring data in ordered time sequences to learn the process dynamics. As has been already said, for the NN training and validation stages, we have extracted 2 118 540 pairs, leaving 10% of the total pixels for the NN cross validation. The target data were organized into 141 236 time sequences of 15 $T_b(x_i, y_j, t_k)$. The training dataset consisted of 127 112 of these sequences, whereas the remaining 14 124 sequences have formed the cross-validation dataset. In this case, the performance indexes have been calculated by replacing the total number of pixels $N_{lat} \times N_{lon}$ in (8)–(10) by $0.9 N_e$ for the training dataset and by $0.1 N_e$ for the test dataset. Moreover, data were simply indexed as $T_b(i)$ with i ranging from 1 to $0.9 N_e$ and from 1 to $0.1 N_e$, depending on the considered dataset.

A. Sensitivity Tests of IR Radiance Field Nowcast

In order to track storm cloud structures at the scale considered here, a typical wind velocity of 20–30 km/h can be assumed. This means that, in 30 min, a cloud structure may be advected of about 10 km. The larger the number of past frames taken into account, the greater should be the extent of the region around the considered x_i, y_j pixel in building the IP. This means that the space and time dimensions, which are described by the input vector sequence $\mathbf{V}(t_1), \dots, \mathbf{V}(t_k)$, are inherently related.

The number of layers $n + 1$ and neurons N_l in each hidden layer and the number of elements N_0 of the input vector can impose some constraints on the synaptic weights w_{ij} . For a three-layer NN, the latter is equal to $(N_0 + N_1) \cdot N_1 + N_1 \cdot N_2$ for the RC-NN and equal to $N_0 \cdot N_1 + N_1 \cdot N_2$ for the FF-NN (see Fig. 5). On the other hand, the number of examples N_e to be provided to the network in the training phase should be generally at least an order of magnitude larger than the number of synaptic weights [21]. The reason for this requirement is to avoid overfitting during training. Of course, the larger the number of neurons (and weights), the larger the ability of the NN to map complex functions, but it also implies a longer computing time required for the training stage and a higher risk to overfit the available data.

In our application, we have chosen a “pruning” approach [20]; designing a redundant NN and then reducing all its parameters in order to find the best performance on the validation dataset in terms of the statistical indexes given in (8)–(10). We have randomly reduced the size of N_e down to 200 000, changed n between two and three, and varied N_l from 100 down to 45. At the same time, the neighbor-contour order n_c has been varied from 10 to 1. The result of this extensive pruning procedure is that three-layer ($n = 2$) NNs have comparable performances with four-layer ($n = 3$) NNs. A number N_e equal to about 240 000 should be optimal for training purposes. For the hidden layer of the three-layer FF-NN, an optimal value of $N_1 = 60$ neurons has been found. For the three-layer RC-NN, the optimal number N_1 of hidden neurons has been found to be equal to 44, a number which also guarantees to maintain a comparable complexity (i.e., similar total number of weights) between the three-layer RC and FF architectures.

In Table I, some results, which are related to the selection of the suitable number of neighbor-contour order n_c , are shown for an RC-NN, having a fixed $N_e = 240 000$. The table indicates that the use of neighbor contours of higher orders (up to $n_c = 8$) can give better performance indexes. However, since the use of higher order neighbor contours also means a longer computing time, we have decided to select, as a compromise, $n_c = 5$ in training the NNs considered in this paper.

In Table II, the best performance indexes of the two neural architectures are reported. Both the NN architectures reached the best cross validation after a few hundred epochs. The

$$m_\varepsilon(t_k) = \frac{1}{N_{lon}N_{lat}} \sum_{i=1}^{N_{lon}} \sum_{j=1}^{N_{lat}} [\hat{T}_b(x_i, y_j, t_k) - T_b(x_i, y_j, t_k)] \quad (8)$$

$$s_\varepsilon(t_k) = \left(\frac{1}{N_{lon}N_{lat}} \sum_{i=1}^{N_{lon}} \sum_{j=1}^{N_{lat}} [\hat{T}_b(x_i, y_j, t_k) - T_b(x_i, y_j, t_k)]^2 \right)^{1/2} \quad (9)$$

$$r_\varepsilon(t_k) = \frac{\sum_{i=1}^{N_{lon}} \sum_{j=1}^{N_{lat}} [\hat{T}_b(x_i, y_j, t_k) - \langle \hat{T}_b(t_k) \rangle] [T_b(x_i, y_j, t_k) - \langle T_b(t_k) \rangle]}{\left(\sum_{i=1}^{N_{lon}} \sum_{j=1}^{N_{lat}} [\hat{T}_b(x_i, y_j, t_k) - \langle \hat{T}_b(t_k) \rangle]^2 \sum_{i=1}^{N_{lon}} \sum_{j=1}^{N_{lat}} [T_b(x_i, y_j, t_k) - \langle T_b(t_k) \rangle]^2 \right)^{1/2}} \quad (10)$$

TABLE I
PERFORMANCE INDEXES AS A FUNCTION OF THE ORDER OF
NEIGHBOR CONTOURS N_C FOR AN RC-NN, USING JANUARY 24,
2003, TRAINING AND VALIDATION SEQUENCE

Order	Pixels	Training data set			Validation data set		
		m_ε	s_ε	r_ε	m_ε	s_ε	r_ε
1	9	0.29	5.45	0.94	0.25	5.69	0.93
3	49	0.36	5.06	0.95	0.31	5.25	0.94
5	121	0.20	4.92	0.95	0.18	5.09	0.95
8	189	0.16	4.87	0.95	0.13	5.03	0.95
10	441	0.28	4.85	0.95	0.27	5.00	0.95

TABLE II
COMPARISON OF PERFORMANCE INDEXES FOR THE RC-NN AND FF-NN,
USING JANUARY 24, 2003, TRAINING AND VALIDATION SEQUENCE

NN type	Training data set			Validation data set		
	m_ε	s_ε	r_ε	m_ε	s_ε	r_ε
RC	0.01	4.04	0.97	-0.10	4.51	0.96
FF	-0.18	4.77	0.96	-0.35	5.16	0.95

RC-NN shows an rmse of about 15% lower than the FF-NN on the training dataset. This margin reduces to about 12.5% on the validation dataset.

As explained before, for a trained RC-NN, the output response to a given IP will depend on the previous network activity. We have investigated how many previous images are required for the RC-NN to perform at an optimal level. It has been found that, in order to “spin up” the RC-NN, we need to use few (usually four to six) previous T_b frames (see Table III). This means that, if we have to apply the RC-NN operationally, it should first run on a few frames before its nowcasting performance reaches the best values in terms of performance indexes. For example, if the first Meteosat-7 satellite image is available at 00:00 GMT, the network response will be optimal after five successive frames, i.e., beginning from 02:30 GMT.

An independent test between the nowcasting capabilities of RC and FF-NNs, which are trained on data extracted from the January 24, 2003, event, was also carried out on a sequence of satellite images from November 25, 2005. This rainfall event was characterized by a widespread intense rainfall over central and south Italy and lasted for about 12 h. The results, which are reported in Table IV, show the better performance of the RC-NN configuration with respect to the FF, even considering an event occurred almost two years later with different seasonal and meteorological conditions.

B. Comparison With Conventional Methods

The performances of the FF and RC neural nowcast methods have been compared with the TIP, SSD, and LTE conventional methods (see Section II-B). To this aim, we have used the test dataset of January 25, 2003, as mentioned in Section IV-C. The performance indexes, which are defined in (8)–(10) and related to both neural configurations and conventional methods, are shown in Table V. This table shows that the SSD method results are slightly better than the TIP method. The LTE method performs quite poorly with respect to the other two methods. The correlation indexes of RC-NN

are larger than those obtained through the conventional methods and the FF-NN configuration. The latter shows the performance indexes closer to the best conventional method ones. This analysis suggests that the RC-NN generalization capability may be probably related to the dynamics description provided to the network during the training stage.

The previous results refer to the entire frame nowcast. Indeed, it is well known that, within clouds and precipitating areas, the IR T_b field is sensitive to the cloud top layers [5]–[14]. This means that colder pixels can be usually associated with rainfall convective and stratiform activity, with some ambiguities with respect to cirrus clouds when using only one IR channel [14]. In place of any cloud and rain masking, we can compare the performance indexes on selected areas (or cyclonic areas) of the “cold” pixels in the nowcasted satellite image, introducing a variable IR threshold T_{b0} on T_b frames. For a given value of T_{b0} , cyclonic contours are isolated such that the lower is T_{b0} , the smaller is the selected cyclonic area.

In Figs. 6 and 7, the correlation diagrams corresponding to the RC-NN and SSD nowcasting techniques are compared on such selected areas for different values of the threshold T_{b0} for a sequence of frames from January 24 and 25, 2003. Both figures display the mean value and the standard deviation of r_ε . Fig. 6 shows that the mean correlation index tends to decrease as the threshold T_{b0} is lowered, both for SSD and RC-NN. The mean correlation indexes are higher for the RC-NN than for the SSD for all threshold T_{b0} values. The standard deviation of RC-NN r_ε remains limited to few percent as long as the threshold T_{b0} is greater than 235 K, whereas it shows a marked increase as T_{b0} reaches or becomes smaller than this limit. Similar results have been obtained on the sequence of January 25.

In Figs. 8 and 9, scatterplots compare the measured IR T_b 's to those obtained from the SSD and RC-NN nowcasting methods, using data from frame 12 (6:00 UTC) of January 24, 2003. Intermediate T_b values show more scatter than higher T_b values, which is consistent with the decrease of correlation with the IR temperature. Despite the superior performance of the RC-NN, we note that very low predicted IR temperatures are affected by a small systematic bias. The NN training algorithm seems to be less able to reproduce extreme values, presumably because of their poor representation in the training sample.

VI. RAINFALL FIELD NOWCASTING

The predicted IR T_b field can be used as input to any rainfall estimation algorithm that is capable of processing the IR satellite data. Both statistical and NN approaches have been developed in recent years [10]–[14]. In this paper, in order to provide rainfall field estimates from the nowcasted IR T_b field, a further NN algorithm has been used [26], [29]. The NN approaches to rainfall retrievals from space have proved to be quite effective techniques, although with some inherent limitations [7], [12], [18], [19].

The NN retrieval algorithm consists of a cascade of two FF-NNs (see Section IV), which are trained with the IR and MW data from SSM/I [26] that are collocated in space and time.

TABLE III
RC NEURAL CONFIGURATION NOWCASTING PERFORMANCE INDEXES WITH A GROWING NUMBER OF ORDERED IPs

IP	1	2	3	4	5	6	7	8	9	10
m_e	-0.035	0.198	0.127	0.120	0.132	0.135	0.134	0.134	0.135	0.135
s_e	4.853	4.318	4.242	4.240	4.227	4.225	4.227	4.227	4.226	4.226
r_e	95.37	96.41	96.54	96.53	96.56	96.56	96.56	96.56	96.56	96.56

TABLE IV
PERFORMANCE INDEXES, DEFINED IN (8)–(10), USING RC AND FF-NNS WITH INPUT FRAME AT TIME T_K (ON THREE DIFFERENT TEST SEQUENCES) TO NOWCAST THE IR RADIANCE MAP AT $T_K + 1$. K INDICATES THE FRAME NUMBER IN THE 48 FRAMES OF THE METEOSAT DAILY SEQUENCE

TIME PERIOD	24/01/03 - $k=3-10$	25/01/03 - $k=3-10$	25/11/05 - $k=26-33$			
NN Type	RC	FF	RC	FF	RC	FF
m_e	0.144	0.396	0.111	0.307	0.480	0.932
s_e	4.218	4.880	5.282	5.808	5.563	5.984
r_e	96.65	95.57	93.69	92.35	94.87	94.21

TABLE V
PERFORMANCE INDEXES COMPARISON ON TWO DIFFERENT SATELLITE FRAME SEQUENCES BETWEEN THE NEURAL AND CONVENTIONAL NOWCASTING METHODS

TIME PERIOD	24/01/03 - $k=3-10$			25/01/03 - $k=3-10$		
Method/Index	m_e	s_e	r_e	m_e	s_e	r_e
RC	0.144	4.218	96.65	0.111	5.282	93.69
FF	0.396	4.880	95.57	0.307	5.808	92.35
SSD	-0.098	5.775	93.74	0.057	6.152	91.87
TIP	-0.096	5.822	93.73	0.110	6.291	91.18
LTE	-0.015	8.643	87.84	0.012	9.343	84.21

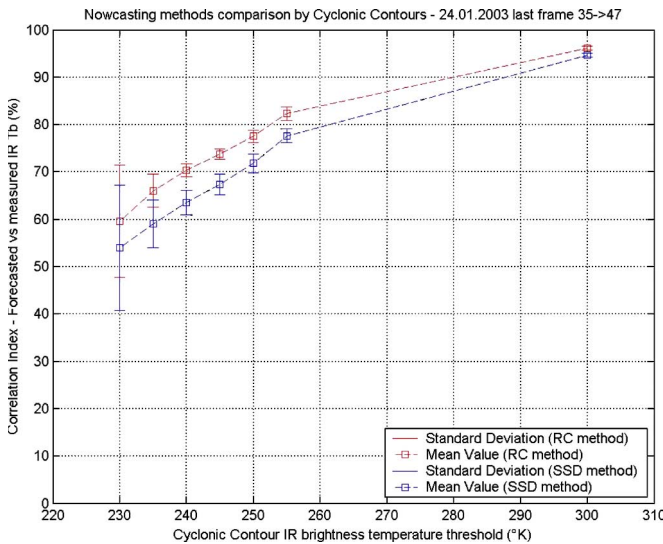


Fig. 6. Nowcasting of the frame $k + 1$, on a sequence of January 24, 2003, analyzed by means of cyclonic contours. Comparison between NeuCAST and SSD methodology mean correlation index and the associated standard deviation for various IR T_b thresholds.

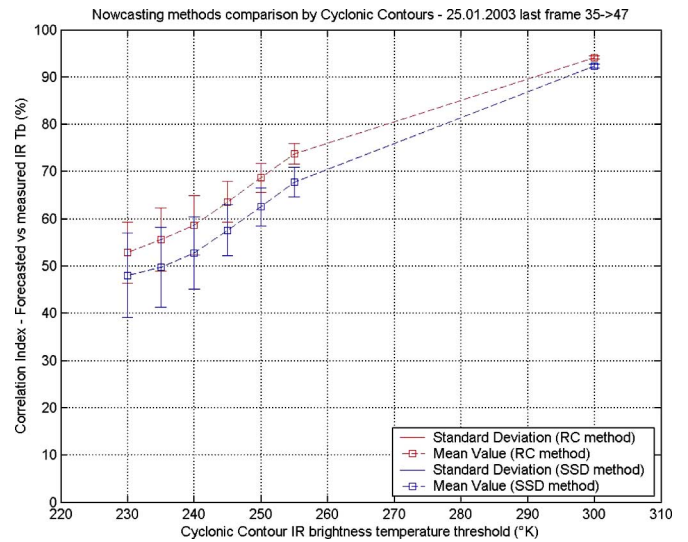


Fig. 7. Same as in Fig. 6 but for January 25, 2003.

Both the IR and MW datasets cover the European Mediterranean region of Fig. 2 during the period from 4:12 UTC to 18:58 UTC on January 24, 2003, for 15 polar orbiting satellite overpasses. Note that, since the spatial resolution of MW data is worse than that of the IR data, a nominal MW field of view generally includes more than one IR pixel (see Section II). For

this reason, a square 5×5 IR pixel grid was matched with an MW field of view. Rain rates from SSM/I were retrieved by using a globally validated regression algorithm applied to the available SSM/I sequences [15].

The rain-rate retrieval procedure is divided into two steps. In the first “masking” step, an FF-NN algorithm is trained to produce a rain/no-rain mask within the domain under consideration (Southern Europe). This is accomplished by using, as inputs,

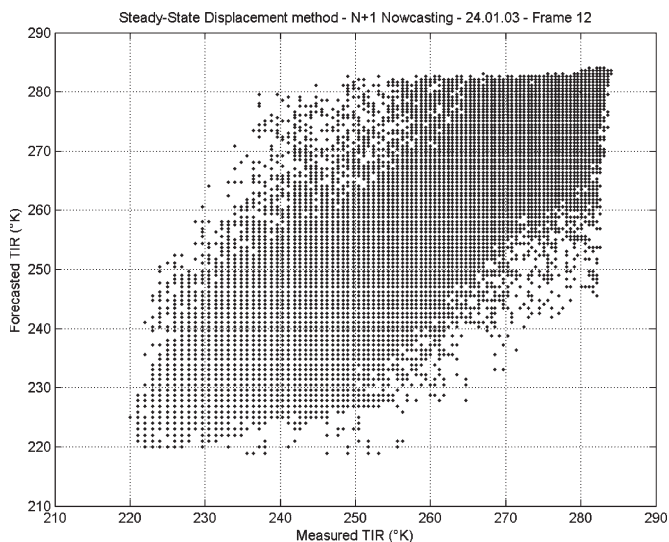


Fig. 8. SSD nowcasting of frame 12 of January 24, 2003, sequence. Forecasted IR T_b compared to the measured IR T_b .

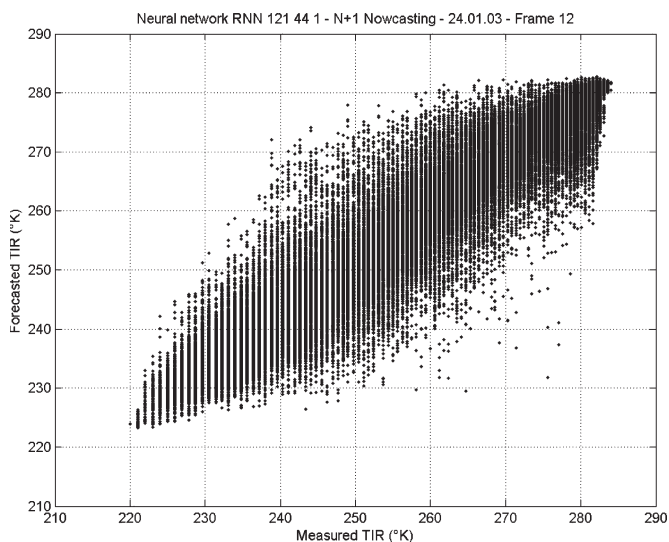


Fig. 9. Same as in Fig. 8 but for the RC-NN methodology.

the IR T_b image and the digital terrain model information of the region under consideration and, as targets, the binary mask obtained from the SSM/I estimated rain-rate map [14]. In the second “inversion” step, the rain-mask output of the previous FF-NN becomes an input of a second FF-NN. The latter has been trained using, as inputs, the IR T_b image texture and the rain mask and, as outputs, only those pixels recognized as rainy pixels and characterized by an SSMI-derived rain rate [26], [29]. After an NN optimization procedure (see Section V-A), a four-layer topology has been chosen for both the FF-NNs. The number N_1 and N_2 of neurons of the two hidden layers has been set to ten and eight, respectively, for both the FF-NNs.

An example of the NeuCAST prediction chain (see Fig. 1) is shown in Figs. 10 and 11. Fig. 10 shows the nowcast of IR T_b field by means of the RC-NN algorithm and its related error for frame 31 on 15:30 GMT on January 24, 2003, using frame 30 of Fig. 2 as the latest available frame. The error is defined

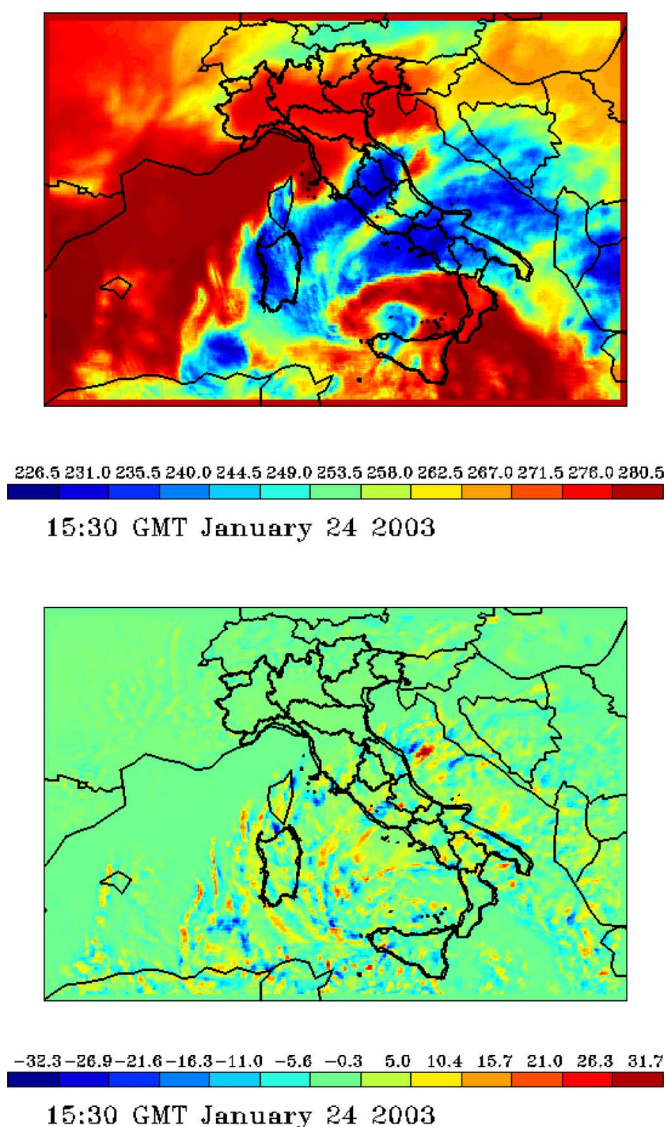


Fig. 10. Example of the RC-NN prediction of IR radiance field at 15:30 GMT (frame 31) on January 24, 2003, using the measured IR T_b image at 15:00 GMT (frame 30) shown in Fig. 2 as the latest available frame. (Top panel) Nowcasted IR T_b field and (bottom panel) estimation error (in kelvin), with respect to the measured IR T_b , are displayed.

as the difference between the nowcasted IR T_b values and the measured ones.

As a second step, Fig. 11 shows the rain-rate field estimated by the FF-NN technique from the nowcasted IR T_b field in Fig. 10. On the bottom panel, the rainfall field difference between the rain-rate estimates derived from the nowcasted IR T_b field and those derived from the corresponding measured IR T_b field is also shown. From Figs. 10 and 11, larger errors are associated with regions where, as expected, spatial discontinuities are more significant as along the warmer pixel clusters embedded within the wide cold area over central Italy. The errors are almost negligible where the clear-air atmospheric conditions tend to prevail, as physically reasonable. The overall error is quite low, representing a percentage error less than 15% with respect to the average range of retrieved rainfall rates from an instantaneous T_b image.

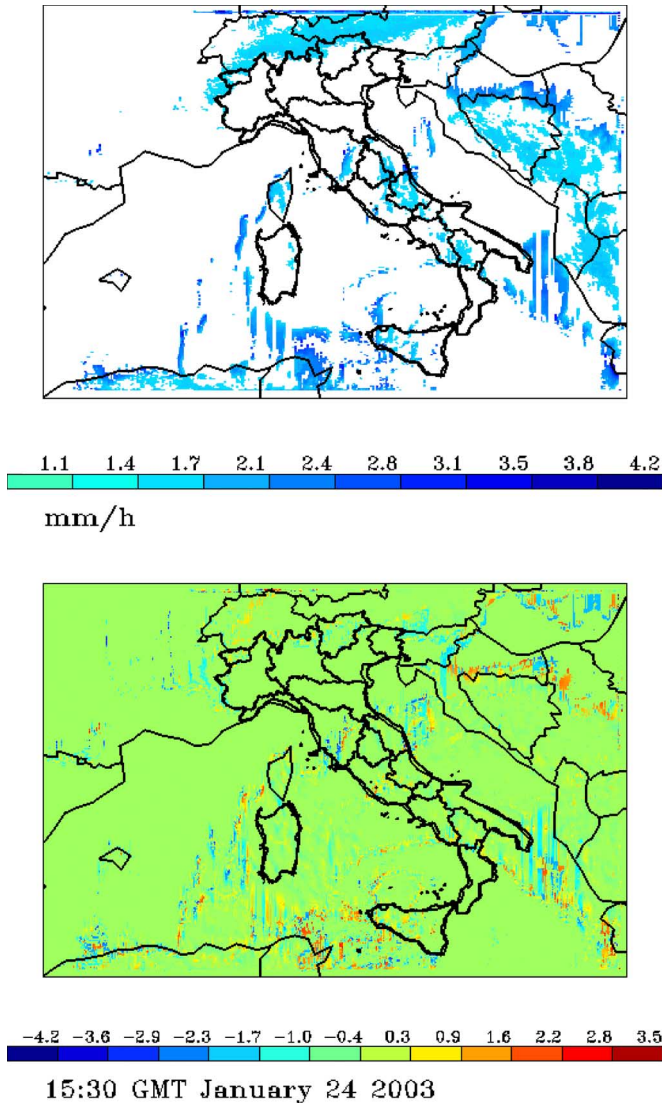


Fig. 11. Example of the NeuCAST prediction of rain-rate field (in millimeters per hour) from the IR nowcasted image of Fig. 10 at 15:30 on January 24, 2003. Rain-rate retrieval from (top panel) the IR nowcasted image and (bottom panel) the estimation error (in millimeters per hour), with respect to the rain-rate estimate from the IR measured image, are displayed.

TABLE VI
ERROR BIAS, *rmse*, *nrmse*, CORRELATION COEFFICIENT, PODNR, PODR,
AND FAR FOR THE RAIN-RATE FIELD, USING RC-NN FOR A SEQUENCE
OF RAIN RATE NOWCASTS OF THE SUBSEQUENT FRAME,
BASED ON FRAMES 3 TO 10 ON JANUARY 25, 2003

Analysis index	Result
<i>Bias</i>	0.001 mm/h
<i>rmse</i>	0.42 mm/h
<i>nrmse</i>	0.87
<i>Corr. Coeff.</i>	0.62
<i>PODNR</i>	0.95
<i>PODR</i>	0.72
<i>FAR</i>	0.30

In order to extend the statistical analysis of rain-rate nowcast error, Table VI shows the performance indexes related to the rain-rate field estimated from the nowcasted IR T_b field with respect to the rain field estimated from the actual IR

T_b field for the test sequence of Meteosat satellite images of January 25, 2003 (frames 3 to 10). Apart from error bias, *rmse*, and correlation coefficient, we have also computed the normalized *rmse* (*nrmse*) defined as the ratio between the *rmse* and the measured rain-rate-field standard deviation. The following rain detection indexes have been evaluated as well: the probability of detection of no rain (PODNR), the probability of detection of rain (PODR), and the false alarm ratio (FAR) defined as in [14]. Table VI suggests that the rainfall *rmse* is about 10% of the maximum rain rate obtained for this event (4 mm/h), and the correlation coefficient of 60% is reasonable for instantaneous estimates. The bias is very low, and the *nrmse* is lower than one, which means that the estimate error is lower than the uncertainty associated to the rain field used as reference. In the same table, the POR and PODNR values are both quite high, whereas FAR is quite low as we desire it to be.

This analysis would suggest that the nowcasted rain-rate field may be not the critical element within the nowcasting-chain error budget. We have assumed here that the combined MW-IR rainfall retrieval algorithm provides the actual rain-rate field. Indeed, this assumption is not true as the SSM/I-derived rain-rate estimates usually show a correlation of about 0.6 with measured rain-gauge fields [5], [30]. Even though this consideration does not affect the NeuCAST methodology, it can have an impact when validating the entire multisatellite nowcast procedure with ground-based measurements to evaluate the overall rain-rate error budget.

VII. CONCLUSION

The objective of this paper has been to apply an NN approach, which is named NeuCAST, to the very short-term prediction of the rainfall field from IR and MW radiometric imagery aboard, respectively, GEO and LEO satellites. The NeuCAST procedure has been divided in two cascade steps. First, the IR radiance field measured from the GEO satellites is projected ahead in time; second, the projected radiance field is used in estimating the rainfall field by means of an MW-IR combined rain retrieval algorithm.

Concerning the first step of NeuCAST prediction, the NN techniques, based on RC and FF architectures, have been proposed and extensively compared. Several three-layer RC and FF neural configurations have been tested, varying the order of neighbor pixel contours, the number of hidden neurons, and the training parameters. The RC-NN configuration is found to be the best performing architecture for the same degree of complexity. The comparison of NN and conventional techniques for the satellite IR brightness temperature image nowcast has shown that the NN approach performs significantly better than any of the three conventional methods considered here. The results indicate that an RC-NN, which is properly designed and trained, can exhibit significant advantages in terms of accuracy with respect to the conventional nowcasting methods. Concerning the second step of NeuCAST retrieval, the predicted IR temperature field has been used as an input for a combined MW-IR rain estimation algorithm. The combined multisatellite algorithm has been based on a

further cascade of FF-NNs, which are trained by space-time colocated IR and MW data, the latter derived from spaceborne MW radiometers (e.g., SSM/I in this paper). The overall error, which is found after the application of the entire NeuCAST prediction chain to some case studies, has been shown to be relatively low and quite encouraging. It should be stressed that the combined MW-IR rainfall retrievals are affected by some inherent errors which have been disregarded here. Even though these errors do not affect the NeuCAST methodology, they may be a significant part of the overall budget of a rainfall nowcasting.

A further improvement in the nowcasting performance of an NN algorithm is expected if a wider set of input/output patterns, which are representative of different meteorological and geographical situations, is provided to the network during the training phase. Another possible way to optimize the forecasting capability of an NN-based system is to use multisensor information at a higher sampling rate, using the MSG data from different multispectral channels with a sampling interval of 15 min. Ground-based radar rain products may also be used as a more accurate source of the rain-rate calibration fields within the NeuCAST retrieval step. Future work will also be focused on the systematic evaluation of the error budget of the MW-IR combined rain estimate algorithms, particularly over land, the NN optimal design for operational use, and the exploitation of the NN approach to predict rain fields more than half an hour in advance.

ACKNOWLEDGMENT

Meteosat data have been archived by CETEMPS, Italy, and provided by EUMETSAT. SSM/Is were kindly provided by NOAA-DAAC, and processed by Dr. D. Cimini of CETEMPS. The authors would like to thank the anonymous reviewers for the helpful comments and suggestions.

REFERENCES

- [1] G. Roth, G. Boni, F. Giannoni, and R. Rudari, "On the role of a hydrologic model in regional precipitation and flood frequency analyses," *EOS, Trans. AGU*, vol. 85, no. 17, p. JA259, 2004.
- [2] F. Siccardi, G. Boni, L. Ferraris, and R. Rudari, "A hydrometeorological approach for probabilistic flood forecast," *J. Geophys. Res.*, vol. 110, no. D5, D05101, Mar. 2004.
- [3] L. Li, W. Schmid, and J. Joss, "Nowcasting of motion and growth of precipitation with radar over a complex orography," *J. Appl. Meteorol.*, vol. 34, no. 6, pp. 1286–1300, Jun. 1995.
- [4] J. W. Wilson, N. A. Crook, C. K. Mueller, J. Sun, and M. Dixon, "Nowcasting thunderstorms: A status report," *Bull. Amer. Meteorol. Soc.*, vol. 79, no. 10, pp. 2079–2099, Oct. 1998.
- [5] F. S. Marzano, A. Mugnai, and J. Turk, "Precipitation retrieval from spaceborne microwave radiometers and combined sensors," in *Remote Sensing of Atmosphere and Ocean From Space*, F. S. Marzano and G. Visconti, Eds. Dordrecht, The Netherlands: Kluwer, 2002, pp. 107–126.
- [6] G. A. Vicente, R. A. Cofield, and W. P. Menzel, "The operational GOES infrared rainfall estimation technique," *Bull. Amer. Meteorol. Soc.*, vol. 79, no. 9, pp. 1883–1898, Sep. 1998.
- [7] K. L. Hsu, X. Gao, S. Sorooshian, and H. V. Gupta, "Precipitation estimation from remotely sensed information using artificial neural networks," *J. Appl. Meteorol.*, vol. 36, no. 9, pp. 1176–1190, Sep. 1997.
- [8] C. Kummerow and L. Giglio, "A method for combining passive microwave and infrared rainfall observations," *J. Atmos. Ocean. Technol.*, vol. 12, no. 1, pp. 33–45, Feb. 1995.
- [9] V. Levizzani, F. Porcù, F. S. Marzano, A. Mugnai, E. A. Smith, and F. Prodi, "Investigating a SSM/I microwave algorithm to calibrate METEOSAT infrared instantaneous rain-rate estimates," *Meteorol. Appl.*, vol. 3, pp. 5–17, 1996.
- [10] S. W. Miller, P. A. Arkin, and R. Joyce, "A combined microwave infrared rain rate algorithm," *Int. J. Remote Sens.*, vol. 22, no. 17, pp. 3285–3307, Nov. 2001.
- [11] T. Bellerby, M. Todd, D. Kniveton, and C. Kidd, "Rainfall estimation from a combination of TRMM Precipitation Radar and GOES multispectral satellite imagery through the use of an artificial neural network," *J. Appl. Meteorol.*, vol. 39, no. 12, pp. 2115–2128, Dec. 2000.
- [12] F. J. Tapiador, C. Kidd, V. Levizzani, and F. S. Marzano, "A neural networks-based PMW-IR fusion technique to derive half hourly rainfall estimates at 0.1° resolution," *J. Appl. Meteorol.*, vol. 43, no. 4, pp. 576–594, Apr. 2004.
- [13] D. I. F. Grimes, E. Coppola, M. Verdecchia, and G. Visconti, "A neural network approach to real time rainfall estimation for Africa using satellite data," *J. Hydrometeorol.*, vol. 4, no. 6, pp. 1119–1133, Dec. 2003.
- [14] F. S. Marzano, M. Palmacci, D. Cimini, G. Giuliani, and J. F. Turk, "Multivariate statistical integration of satellite infrared and microwave radiometric measurements for rainfall retrieval at the geostationary scale," *IEEE Trans. Geosci. Remote Sens.*, vol. 42, no. 5, pp. 1018–1032, May 2004.
- [15] R. R. Ferraro, "SSM/I derived global rainfall estimates for climatological applications," *J. Geophys. Res.*, vol. 102, no. D14, pp. 16715–16735, 1997.
- [16] S. Di Michele, A. Tassa, A. Mugnai, F. S. Marzano, P. Bauer, and J. P. V. P. Baptista, "Bayesian algorithm for microwave-based precipitation retrieval: Description and application to TMI measurements over ocean," *IEEE Trans. Geosci. Remote Sens.*, vol. 43, no. 14, pp. 778–791, Apr. 2005.
- [17] F. Dell'Acqua and P. Gamba, "Pyramidal rain field decomposition using radial basis function neural networks for tracking and forecasting purposes," *IEEE Trans. Geosci. Remote Sens.*, vol. 41, no. 4, pp. 853–862, Apr. 2003.
- [18] G. Rivolta, F. S. Marzano, E. Coppola, and M. Verdecchia, "Artificial neural-network technique for precipitation nowcasting from satellite imagery," *Adv. Geosci.*, vol. 7, pp. 97–103, 2006.
- [19] F. J. Tapiador, C. Kidd, K. L. Hsu, and F. S. Marzano, "Neural networks in satellite rainfall estimation," *Meteorol. Appl.*, vol. 11, no. 1, pp. 1–9, Mar. 2004.
- [20] S. Haykin, *Neural Networks: A Comprehensive Foundation*, 2nd ed. Englewood Cliffs, NJ: Prentice-Hall.
- [21] R. Hecht-Nielsen, *Neurocomputing*. Reading, MA: Addison-Wesley, 1991.
- [22] L. J. Elman, "Finding structure in time," *Cogn. Sci.*, vol. 14, no. 2, pp. 179–211, Apr.–Jun. 1990.
- [23] R. Ferretti and C. Faccani, "Data assimilation of high density observations—Part II: Impact on the forecast of the precipitation for the MAP/SOP IOP2b," *Q. J. R. Meteorol. Soc.*, vol. 131A, no. 605, pp. 43–62, Jan. 2005.
- [24] C. Faccani, D. Cimini, R. Ferretti, F. S. Marzano, and A. C. Taramasso, "3DVAR assimilation of SSM/I data over the sea for the IOP2 MAP case," *Adv. Geosci.*, vol. 2, pp. 229–235, 2005.
- [25] J. Hollinger, J. Peirce, and G. Poe, "SSM/I instrument evaluation," *IEEE Trans. Geosci. Remote Sens.*, vol. 28, no. 5, pp. 781–790, Sep. 1990.
- [26] F. S. Marzano, D. Cimini, E. Coppola, M. Verdecchia, V. Levizzani, F. Tapiador, and J. F. Turk, "Satellite radiometric remote sensing of rainfall fields: Multi-sensor retrieval techniques at geostationary scale," *Adv. Geosci.*, vol. 2, pp. 267–272, 2005.
- [27] M. Verdecchia, G. Visconti, F. D'Andrea, and S. Tibaldi, "A neural network approach for blocking recognition," *Geophys. Res. Lett.*, vol. 23, no. 16, pp. 2081–2084, 1996.
- [28] C. Darken and J. Moody, "Towards faster stochastic gradient search," in *Advances in Neural Information Processing Systems 4*. San Mateo, CA: Morgan Kaufmann, 1991, pp. 1009–1016.
- [29] E. Coppola, D. I. F. Grimes, M. Verdecchia, and G. Visconti, "Validation of improved TAMANN neural network for operational satellite-derived rainfall estimation in Africa," *J. Appl. Meteorol.*, vol. 45, no. 11, pp. 1557–1572, Nov. 2006.
- [30] N. Pierdicca, L. Pulvirenti, F. S. Marzano, G. d'Auria, P. Basili, and P. Ciotti, "Intercomparison of inversion algorithms to retrieve rain-rate from SSM/I by using an extended validation set over the Mediterranean area," *IEEE Trans. Geosci. Remote Sens.*, vol. 42, no. 10, pp. 2226–2239, 2004.



Frank Silvio Marzano (S'89–M'99–SM'03) received the Laurea degree (*cum laude*) in electrical engineering and the Ph.D. degree in applied electromagnetics from the University of Rome "La Sapienza," Rome, Italy, in 1988 and 1993, respectively.

In 1993, he collaborated with the Institute of Atmospheric Physics, National Research Council (CNR), Rome. From 1994 to 1996, he was with the Italian Space Agency, Rome, as a Postdoctorate Researcher. After working as a Lecturer with the University of Perugia, Perugia, Italy, in 1997, he joined the Department of Electrical Engineering and cofounded the Center of Excellence (CETEMPS), University of L'Aquila, L'Aquila, Italy, coordinating the Satellite and Radar Remote Sensing Laboratory. In 2005, he joined the Department of Electronic Engineering, University of Rome "La Sapienza," where he currently teaches courses on antennas, propagation, and remote sensing. His current research interests include passive and active remote sensing of the atmosphere from ground-based, airborne, and spaceborne platforms, particularly focusing on precipitation using microwave and infrared data, development of inversion methods, radiative transfer modeling of scattering media, and radar meteorology issues. He is also involved in radiopropagation topics in relation to incoherent wave modeling, scintillation prediction, and rain fading analysis along satellite microwave links.

Dr. Marzano was the recipient of the Young Scientist Award of the XXIV URSI General Assembly in 1993 and the ARPAD award from NRL Washington, DC, in 1998. Since 2001, he has been the Italian National Delegate for the European COST actions 720 and 280. Since January 2004, he has been an Associate Editor of the IEEE GEOSCIENCE AND REMOTE SENSING LETTERS.



Giancarlo Rivolta received the M.S. degree in physics (*Laurea Magistralis*) from the University of L'Aquila, L'Aquila, Italy, in 2004. He is currently working toward the Ph.D. degree in environmental monitoring technology at the University of Rome "La Sapienza," Rome, Italy.

Since 2004, he has been with the Center of Excellence CETEMPS, University of L'Aquila, and in 2005, he has been with the Department of Electronic Engineering, University of Rome "La Sapienza," Italy. Before joining the CETEMPS Group, he has worked for 15 years in the electronics industry, mostly with multinational companies, as a Technical Manager. His current research is in the field of passive remote sensing of the atmosphere from spaceborne platforms, with a specific focus on nowcasting methods based on neural networks.



Erika Coppola received the Laurea degree in physics from the University of L'Aquila, L'Aquila, Italy, in 1998, and the Ph.D. degree in meteorology from the University of Reading, Reading, U.K., in 2004.

Since 2002, she has been with the CETEMPS Center of Excellence, University of L'Aquila. Her current research involves passive remote sensing of the atmosphere from spaceborne platforms, with a particular focus on precipitation using microwave and infrared data, and development of inversion neural-network based methods. She is also involved in the hydrological model research activity and development going on in the CETEMPS Hydrological Model Group. She is involved in the coupling of the hydrological model with a regional climate model for land-use impact studies and climate change studies. She works with AGCM model output for climate change studies, and she investigated the change in regime in future climate of the main atmospheric patterns.



Barbara Tomassetti received the Laurea degree in physics from the University of L'Aquila, L'Aquila, Italy, and the Ph.D. degree in physics from the University of L'Aquila.

Since 2002, she has been with the CETEMPS Center of Excellence, University of L'Aquila. Her current research involves the development of inversion methods neural network based, hydrological modeling, and hydrometeorological effects of land use change at regional scale.



Marco Verdecchia received the Laurea degree in physics from the University of L'Aquila, L'Aquila, Italy.

He has been several times at CERN, Geneva (CH), as a Visiting Scientist between 1992 and 1996. Since 2000, he has been a Researcher with the Physics Department and the CETEMPS Center of Excellence, University of L'Aquila. His current research involves remote sensing of precipitation from satellites, development of inversion neural-network based methods, and hydrological modeling and implementation. His main area of interest is the applications of biological algorithms in numerical modeling of complex physics system.